Communication

Effects of Effective Dendrite Size on Dynamic Tensile Properties of Ti-Based Amorphous Matrix Composites

CHANGWOO JEON, JAEYEONG PARK, CHOONGNYUN PAUL KIM, HYOUNG SEOP KIM, and SUNGHAK LEE

In this study, dynamic tensile properties of dendrite-containing Ti-based amorphous matrix composites were examined, and effects of dendrite size on dynamic deformation were investigated. The composites contained 73 to 76 vol pct of dendrites whose effective sizes were varied from 63 to 103 μm. The dynamic tensile test results indicated that the ultimate tensile strength increased up to 1.25 GPa, whereas the elongation decreased to 1 pct, although the overall strength and elongation trends followed those of the quasi-static tensile test. According to the observation of dynamic tensile deformation behavior, very few deformation bands were observed beneath the fracture surface in the composite containing large dendrites. In the composite containing small dendrites, deformation bands initiated inside small dendrites propagated into adjacent dendrites through the amorphous matrix, and were crossly intersect perpendicularly in widely deformed areas, which beneficially worked for elongation as well as strength.

DOI: 10.1007/s11661-016-3349-2

Remarkable advances in bulk amorphous alloys have been made by developing amorphous alloys with high amorphous-forming ability *via* conventional casting methods,[1–9] but problems such as brittle fracture need to be solved for their wider applications.[10–13] In order to overcome this brittle fracture problem, Zr- or Ti-based amorphous matrix composites have been actively developed by homogeneously distributing ductile crystalline dendrites of β phase in the amorphous matrix.[14–19]

When ductile dendrites are homogeneously distributed in the amorphous alloy matrix, the ductility of composites under quasi-static tensile or compressive loading can be dramatically enhanced over that of monolithic amorphous alloys, while keeping the basic advantages of high strength and stiffness.[15–17,20] Though the information on dynamic deformation of amorphous alloys and their composites can be effectively applied to defense, electrical, and precision machinery industries, phenomena occurring under dynamic loading are rarely investigated. Under dynamic loading, the resistance to deformation or fracture is generally reduced in comparison with quasi-static loading cases, and localized deformation often occurs in a highly narrowed region.[21–25] According to Qiao *et al.*[26] on the dynamic compressive behavior of Zr-based amorphous alloys, multiple shear bands were not sufficiently formed under dynamic loading, which resulted in lower plastic strains than those measured under quasi-static loading. Jeon *et al.*[27] investigated the dynamic compressive behavior of Ti-based amorphous composites, and found that dendrites played an important role in improving the ductility by forming deformation bands. Thus, studies of dynamic deformation are essentially needed for alloy development and process control in high-speed manufacturing, but only limited information is available. In addition, how the abrupt deformation behavior of dendrites under dynamic compressive loading differs from that under dynamic tensile loading has hardly been investigated.

In this study, dendrite-containing Ti-based amorphous matrix composites were fabricated by adding amorphous-forming alloying elements of into a conventional Ti-6Al-4V alloy.[28] The effective size of dendrites was varied by the addition of alloying elements, while the size and volume fraction of dendrites were almost maintained in the three alloys. Dynamic tensile properties were evaluated at a strain rate of about 10^3 s^{-1} using a split Hopkinson tension bar, and deformation mechanisms were analyzed by focusing on how the effective dendrite size affected the initiation and propagation of deformation bands inside dendrites.

Three Ti-based amorphous matrix composites were fabricated in a water-cooled copper crucible by a vacuum arc melting method under a Ti-gettered argon atmosphere after the addition of Ti, Zr, V, Ni, Al, and Be into a Ti-6Al-4V alloy (nominal chemical composition: Ti-6Al-4V-0.1O-0.02N-0.04C (wt pct)). The amount of the Ti-6Al-4V alloy is 18 wt pct, and added alloying elements as well as the overall chemical compositions are shown in Table I. The T1 composite has the basic Ti-Zr-V-Ni-Al-Be composition, and the T2 and T3 composites contain lower contents of Al and Be

CHANGWOO JEON, Postdoctoral Research Associate, JAEYEONG PARK, Research Assistant, CHOONGNYUN PAUL KIM, Research Professor, and HYOUNG SEOP KIM and SUNGHAK LEE, Professors, are with the Center for Advanced Aerospace Materials, Pohang University of Science and Technology, Pohang 790-784, Korea. Contact e-mail: shlee@postech.ac.kr HYOUNG SEOP KIM and SUNGHAK LEE, Professors, are also with the Materials Science and Engineering, Pohang University of Science and Technology, Pohang 790-784, Korea.

Manuscript submitted July 26, 2015.
Article published online February 1, 2016

Table I. Chemical Compositions of the Ti-Based Amorphous Matrix Composites (Wt Percent)

Composite	Percent	Ti-6Al-4V	Ti	Zr	V	Ni	Al	Be
T1	wt pct	18 (–)	37.1 (53.7)	29.9 (29.9)	9 (9.8)	3.5 (3.5)	0.5 (1.1)	2 (2)
T2	wt pct	18 (–)	37.4 (53.9)	30 (30)	9 (9.9)	3.5 (3.5)	0.3 (0.9)	1.8 (1.8)
T3	wt pct	18 (–)	37.7 (54.1)	30.2 (30.2)	9 (10)	3.5 (3.5)	0.1 (0.7)	1.5 (1.5)

(); the overall chemical compositions.

than the T1 composite. The composites were held at 1073 K to 1173 K (800 °C to 900 °C) for 30 minutes and quenched to sufficiently obtain the amorphous matrix.

The Ti-based amorphous composites were electro-polished by a twin-jet polisher (model; Tenupol-5, Struers, Denmark) in an etchant of 60 pct 2-butoxy ethanol + 35 pct methanol + 5 pct perchloric acid, and were observed by a scanning electron microscope (SEM, model; JSM-6330F, Jeol, Japan). The volume fraction and size of dendrites were measured by an image analyzer (model; SigmaScan Pro ver 4.0, Jandel Scientific Co., USA). The electron back-scatter diffraction (EBSD) analysis (resolution; 1 μm) was performed by a field emission scanning electron microscope (FE-SEM, model; Helios NanolabTM, FEI, USA).

The composites were machined into plate-type tensile specimens (gauge length; 6 mm, gauge width; 2.5 mm, gauge thickness; 1.25 mm). The dynamic tensile test was conducted on composite tensile specimens using a split Hopkinson tension bar. The specimen was situated between the input and output bars, and was loaded by a striker bar (diameter; 19 mm) projected at a high speed using an air pressure of 0.2 MPa. Strain rate was controlled by varying the firing pressure. During the dynamic tension, the incident wave, reflective wave, and transmitted wave were measured using strain gages, and recorded at an oscilloscope. Among the recorded waves, the average tensile strain rate as a function of time was calculated from the reflected wave, while the tensile stress as a function of time was calculated from the transmitted wave. Dynamic tensile stress–strain curves were obtained from these two parameters by eliminating the time variable. Tensile strain rate was about 10^3 s^{-1}. Detailed descriptions of the dynamic tensile test are provided in references.[29–33] After the test, fracture surfaces were examined using an SEM.

SEM micrographs of the T1, T2, and T3 composites are shown in Figures 1(a) through (c). β-phase dendrites are homogeneously distributed in the amorphous matrix. The volume fraction and size of dendrites of the three composites are similar in the range of 74 to 76 pct and 24 to 28 μm, respectively.[28] Figures 2(a) through (c) show EBSD inverse pole figure (IPF) color maps. When boundaries between dendrites having orientations differing by 15 deg or higher are considered as high-angle ones, they are regarded as effective dendrite boundaries. Effective dendrite sizes are much larger than dendrite sizes of SEM micrographs [Figures 1(a) through (c)] because effective dendrites having the same orientations are three-dimensionally interconnected. The effective dendrite sizes measured

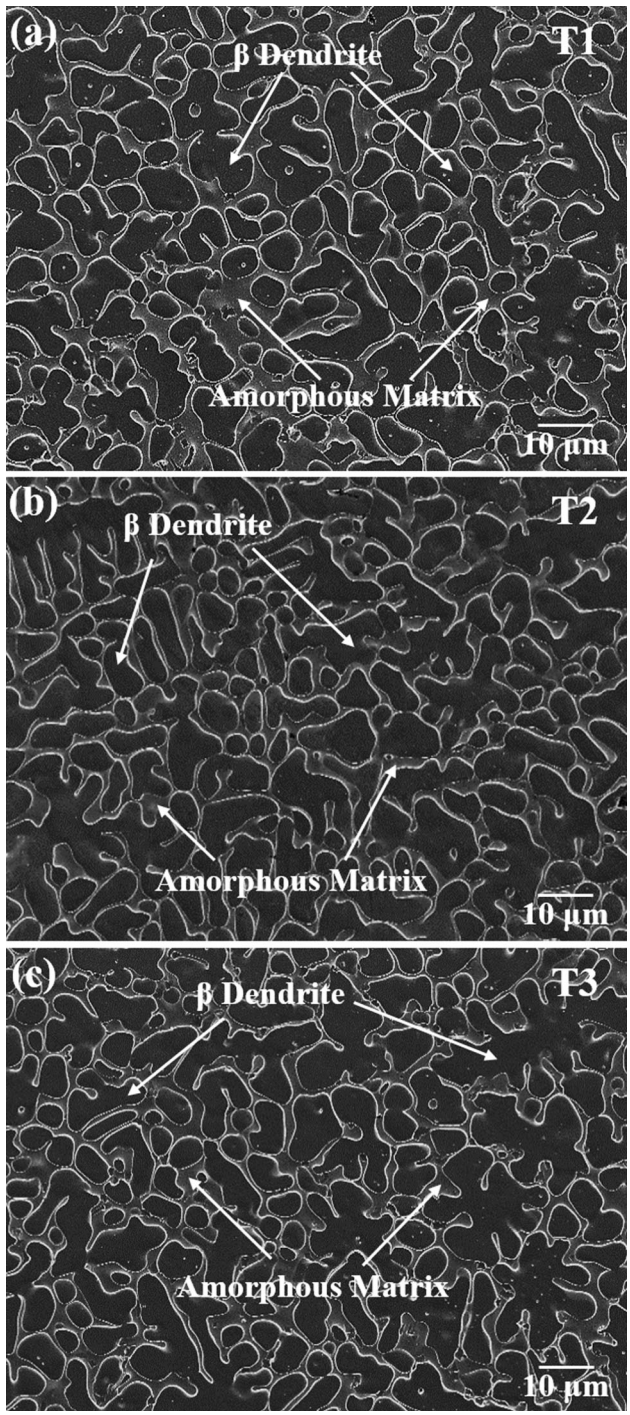

Fig. 1—SEM micrographs of the (*a*) T1, (*b*) T2, and (*c*) T3 composites. β-phase dendrites are homogeneously distributed in the amorphous matrix.

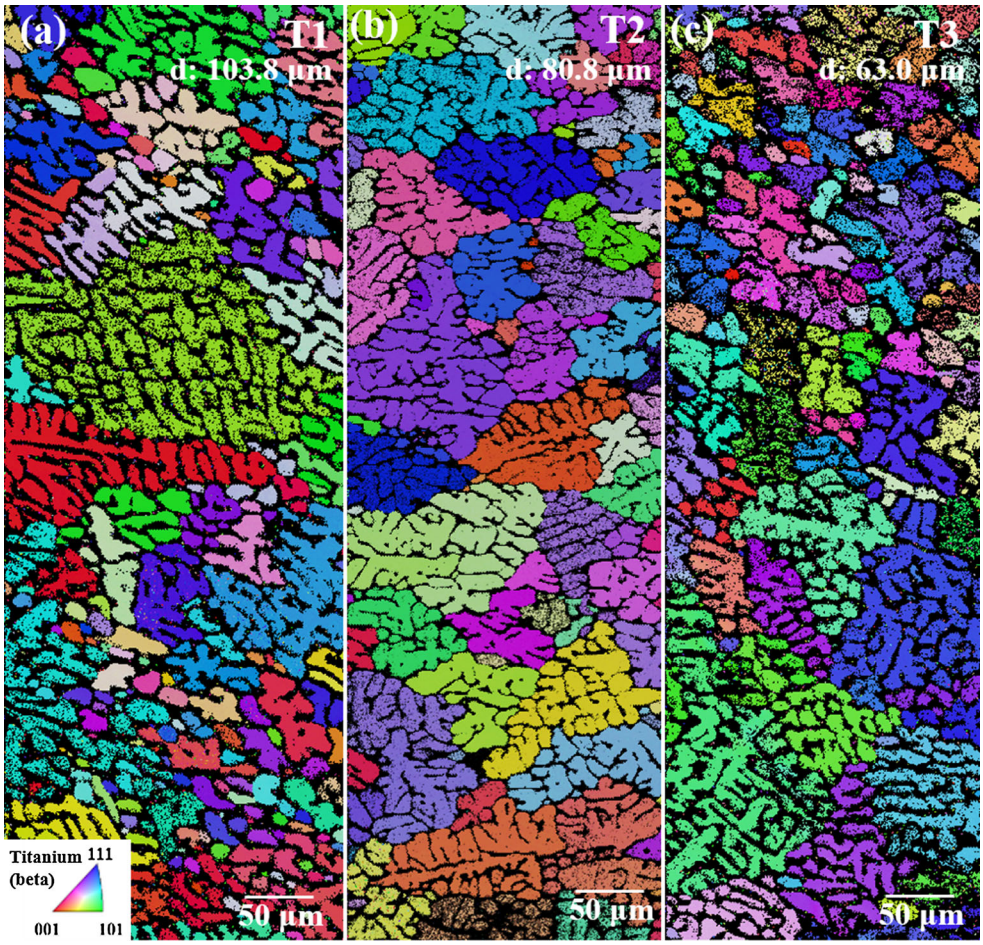

Fig. 2—EBSD inverse pole figure (IPF) color maps of the (*a*) T1, (*b*) T2, and (*c*) T3 composites. Effective dendrite sizes measured from IPF maps are much larger than dendrite sizes of SEM micrographs (Figs. 1(a) through (c)) because effective dendrites having the same orientations are three-dimensionally interconnected.

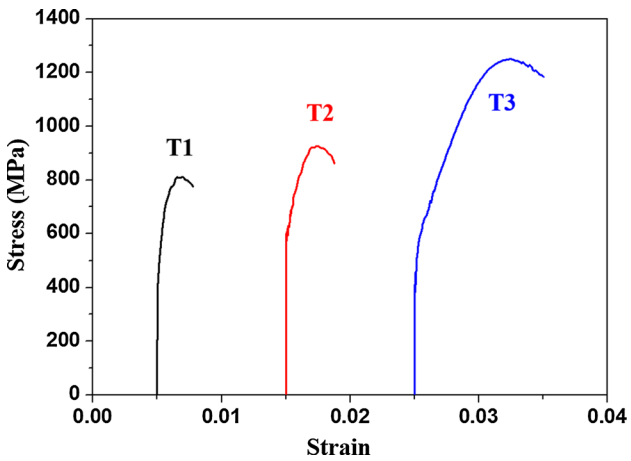

Fig. 3—Dynamic tensile stress–strain curves of the Ti-based amorphous matrix composites. Yield strength cannot be accurately determined.

from the maps are 103.8, 80.8, and 63.0 μm for the T1, T2, and T3 composites, respectively.

Figure 3 shows dynamic tensile stress–strain curves of the three composites, and the tensile test results are summarized in Table II. The yield strength cannot be accurately determined. The yield strength, ultimate tensile strength, and elongation previously obtained from quasi-static tensile tests are also listed in Table II. The ultimate tensile strength and elongation of the T1 composite are 809 MPa and 0.2 pct, respectively. The T2 composite shows similar tensile behavior to the T1 composite, while the properties of the T2 composite are slightly higher. The ultimate tensile strength and elongation of the T3 composite are the best among the three composites, but its elongation reaches only 1 pct. The ultimate tensile strength and elongation measured from the dynamic test are lower than those measured from the quasi-static test. In particular, the elongation is far lower, although the overall trends of strength and elongation follow those of the quasi-static tensile test. Fracture proceeds rapidly, and thus the elongation is very low (0.2 to 1.0 pct).

Figures 4(a) and (b) show SEM fractographs of the dynamically fractured tensile specimens of T1 and T3 composites. In the T1 composite, cleavage-like facets, vein patterns, and smooth patterns are mixed together as marked by arrows in Figure 4(a), whereas ductile dimples are not found. Inside cleavage-like facets,

lamellar patterns composed of many parallel lines can be seen. These are called 'lamellar cleavage patterns' in previous studies on Ti-based amorphous composites.[34] Lamellar cleavage patterns originate from dendritic areas, while vein and smooth patterns originate from amorphous matrix regions.[34] The spacing of lamellar cleavage patterns is about 1 μm. Lamellar cleavage patterns are parallel inside some dendrites, and the other lamellar patterns are vertically formed. Smooth patterns occurring in amorphous matrix regions can be recognized as a more brittle fracture mode than vein patterns because of their flat and smooth shape.[35,36] The fracture surface of the T3 composite is composed of ductile dimples, lamellar cleavage patterns, and vein patterns [Figure 4(b)]. As the spacing of lamellar cleavage patterns increases further to 3 μm, some of lamellar cleavage patterns tend to change to large and elongated dimples, which prevail in dendrite areas.

High magnification images of the deformed areas beneath the fracture surface are presented in Figures 4(c) and (d). Detailed shapes of dendrites can just be seen on the deformed surface. In the T1 composite, the deformation bands are not well developed because very few slip lines are found [indicated by arrows in Figure 4(c)]. Many deformation bands are homogeneously developed in wide areas in the T3 composite (Figure 4(d)). Most of them intersect each other, at angles of about 90 deg, implying β dendrites of a bcc structure.[15,28] The number and density of deformation bands are the highest, indicating that the T3 composite is the most homogeneously deformed. Some slip lines become more pronounced as the deformation proceeds further.

Since the composites show different dynamic tensile properties as well as different deformation and fracture behavior depending on the effective dendrite size, the effects of dendrite size on dynamic tensile behavior should be investigated in detail. Under dynamic tensile loading, when the T1 and T3 composites (effective dendrite size; 103 *vs* 63 μm) are compared, both strength

Table II. Quasi-Static and Dynamic Tensile Test Results of the Ti-Based Amorphous Matrix Composites

Composite	Tensile Loading Mode	Yield Strength (MPa)	Ultimate Tensile Strength (MPa)	Elongation (Percent)
T1	quasi-static	1394 ± 61	1485 ± 72	3.2 ± 1.2
	dynamic	—	809 ± 220	0.2
T2	quasi-static	1443 ± 61	1511 ± 63	5.2 ± 0.8
	dynamic	—	925 ± 189	0.3
T3	quasi-static	1409 ± 25	1498 ± 55	7.1 ± 0.8
	dynamic	–	1245 ± 159	1.0

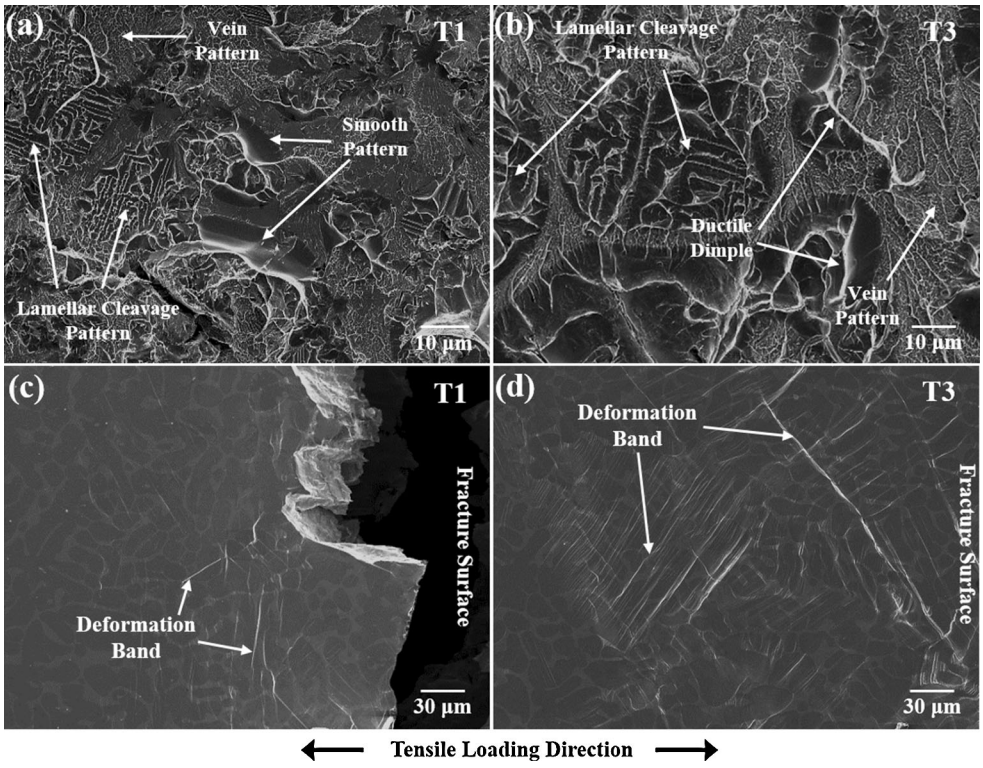

Fig. 4—SEM fractographs of the dynamically fractured tensile specimens of the (*a*) T1 and (*b*) T3 composites and SEM micrographs of the deformed area beneath the fracture surface of the dynamically fractured tensile specimen of the (*c*) T1 and (*d*) T3 composites.

and elongation of the T1 composite are lower than those of the T3 composite (Table II). In the T1 composite, very few deformation bands are formed inside very large dendrites, and cracks are more readily formed at one or two deepened slip lines (Figure 4(c)). As a result, the T1 composite hardly shows plastic deformation. Its fracture modes consist of lamellar cleavage patterns originating from dendrite areas and vein and smooth patterns originating from amorphous matrix regions (Figure 4(a)) as the fracture proceeds in brittle modes. Many deformation bands are formed inside dendrites in several directions in the T3 composite [Figure 4(d)]. Deformation bands initiated inside small dendrites propagate into adjacent dendrites through the amorphous matrix, and intersect perpendicularly in widely deformed areas. Thus, the number and density of deformation bands in the T3 composite are higher than those of the T1 composite. This difference in tensile deformation behavior in the T1 and T3 composites is mainly associated with the dendrite size because the tensile elongation can be improved when dendrites are smaller than a certain size level, and the wide deformation in the T3 composite beneficially works for the improved tensile elongation. As a result, the spacing of lamellar cleavage patterns largely increases to form large and elongated dimples, which prevails in dendrite areas, while smooth patterns disappear in amorphous matrix areas [Figure 4(b)].

According to Jeon *et al.*,[34] the lamellar cleavage fracture is a kind of cleavage fracture modes occurring in bcc materials, and lamellar patterns are spaced in an almost same interval. The orientation difference of dendrites or effective dendrite size importantly influences the appearance of ductile dimpled fracture or lamellar cleavage fracture, and consequently leads to the ductile to brittle transition (ductile dimpled fracture → lamellar cleavage fracture → ordinary cleavage fracture) in dendrite areas. This ductile to brittle transition phenomenon produced by increase in dendrite size can be explained by the appearance of deformation bands and their number and density. In coarse-dendrite-containing T1 composite, coarse dendrites tend to be independently deformed, which leads to inhomogeneous deformation.[28,37] In the fine-dendrite-containing T3 composite, on the other hand, the rather homogenous deformation occurs in dendrites, like in fine-grained materials,[38,39] which improves elongation. Thus, the dendrite size acts as a major parameter affecting the ductile to brittle transition.

The T3 composite shows an elongation of 1.0 pct, although a considerable number of deformation bands are formed. The number and density of deformation bands are much lower than those under quasi-static loading.[28] This is because the time needed for sufficiently forming deformation bands is not enough to go through all the various deformation processes such as formation of deformation bands. Since deformation bands tend to be more localized under dynamic loading than under quasi-static loading, the deformed area is narrower [Figures 4(c) and (d)][37]. This also acts as a reason for the reduced elongation under dynamic loading. In addition, the ultimate tensile strength is lower under dynamic loading than under quasi-static loading (Table II), which is the opposite to the observation that conventional metals or composites show higher strengths under dynamic loading because of the strain rate strengthening effect.[31,40] This is because the three composites abruptly fracture within the elastic range as the resistance to fracture under dynamic loading drops. In this case, the ultimate tensile strength is proportional to the elongation, which is well matched with the present dynamic tensile test results (Table II).

These results for the dendrite-containing Ti-based amorphous composites can be useful in understanding the quasi-static and dynamic deformation behavior and to suggest optimal effective dendrite size for improving the tensile ductility as well as strength. Since deformation bands are well developed inside relatively small dendrites, there exists an optimum size of dendrites, *e.g.*, 63 μm. Since the T3 composite has good properties of high strength and ductility even under dynamic tensile loading, it presents desirable possibilities for overcoming the shortcoming of catastrophically brittle dynamic fracture, while keeping the basic advantages of amorphous alloys and composites.

This work was supported by the National Research Foundation of Korea (NRF) Grant (No. 2014M3C1A9060722) funded by the Ministry of Science, ICT, and Future Planning, Korea and by Brain Korea 21 PLUS Project for Center for Creative Industrial Materials.

REFERENCES

1. W. Chen, Y. Wang, J. Qiang, and C. Dong: *Acta Mater.*, 2003, vol. 51, pp. 1899–1907.
2. M. Kim, S.-W. Kim, S.-H. Yoon, and S. Yi: *Korean J. Met. Mater.*, 2014, vol. 52, pp. 129–35.
3. Y.C. Kim, J.M. Park, J.K. Lee, D.H. Bae, W.T. Kim, and D.H. Kim: *Mater. Sci. Eng. A*, 2004, vols. 375–377, pp. 749–53.
4. J.G. Lee, D.-G. Lee, S. Lee, and N.J. Kim: *Metall. Mater. Trans. A*, 2004, vol. 35A, pp. 3753–61.
5. S.J. Choi, H.S. Lee, J.W. Jang, and S. Yi: *Met. Mater. Int.*, 2014, vol. 20, pp. 1053–57.
6. J.G. Lee, S.S. Park, D.G. Lee, S. Lee, and N.J. Kim: *Intermetallics*, 2004, vol. 12, pp. 1125–31.
7. R. Busch, A. Masuhr, and W.L. Johnson: *Mater. Sci. Eng. A*, 2001, vols. 304–306, pp. 97–102.
8. S.C. Yoon, S.G. Moon, K.Y. Sohn, and W.-W. Park: *Korean J. Met. Mater.*, 2014, vol. 52, pp. 649–55.
9. J.M. Park, H.J. Chang, K.H. Han, W.T. Kim, and D.H. Kim: *Scripta Mater.*, 2005, vol. 53, pp. 1–6.
10. G. Li, M.Q. Jiang, F. Jiang, L. He, and J. Sun: *Mater. Sci. Eng. A*, 2015, vol. 625, pp. 393–402.
11. C.A. Pampillo: *Scripta Metall.*, 1972, vol. 6, pp. 915–17.
12. D.E. Polk and D. Turnbull: *Acta Metall.*, 1972, vol. 20, pp. 493–98.
13. S. Jung, J. Do, D.-G. Lee, B.-J. Lee, G.-U. Cha, and S. Lee: *Met. Mater. Int.*, 2014, vol. 20, pp. 577–83.
14. D.J. Ha, C.P. Kim, and S. Lee: *Mater. Sci. Eng. A*, 2012, vol. 558, pp. 558–65.
15. D.C. Hofmann, J.-Y. Suh, A. Wiest, G. Duan, M.-L. Lind, M.D. Demetriou, and W.L. Johnson: *Nature*, 2008, vol. 451, pp. 1085–89.

16. Y.S. Oh, C.P. Kim, S. Lee, and N.J. Kim: *Acta Mater.*, 2011, vol. 59, pp. 7277–86.
17. C.C. Hays, C.P. Kim, and W.L. Johnson: *Phys. Rev. Lett.*, 2000, vol. 84, pp. 2901–04.
18. C.C. Hays, C.P. Kim, and W.L. Johnson: *Mater. Sci. Eng. A*, 2001, vols. 304–306, pp. 650–55.
19. F. Szuecs, C.P. Kim, and W.L. Johnson: *Acta Mater.*, 2001, vol. 49, pp. 1507–13.
20. L.-F. Wang, X. Cui, Q.-D. Zhang, and F.-Q. Zu: *Met. Mater. Int.*, 2014, vol. 20, pp. 669–76.
21. K.-M. Cho, S. Lee, S.R. Nutt, and J. Duffy: *Acta Metall. Mater.*, 1993, vol. 41, pp. 923–32.
22. K.A. Hartley, J. Duffy, and R.H. Hawley: *J. Mech. Phys. Solids*, 1987, vol. 35, pp. 283–301.
23. D.-K. Kim, S. Kang, S. Lee, and K. Lee: *Metall. Mater. Trans. A*, 1999, vol. 30A, pp. 81–92.
24. D.-G. Lee, S. Lee, and C.S. Lee: *Mater. Sci. Eng. A*, 2004, vol. 366, pp. 25–37.
25. M.W. Lee, H.J. Shin, S.H. Hong, J.T. Kim, H. Choi-Yim, Y. Seo, W.H. Lee, P. Yu, M. Qian, J.K. Lee, and K.B. Kim: *Met. Mater. Int.*, 2014, vol. 20, pp. 1–5.
26. J.W. Qiao, P. Feng, Y. Zhang, Q.M. Zhang, and G.L. Chen: *J. Alloy. Compd.*, 2009, vol. 486, pp. 527–31.
27. C. Jeon, C.P. Kim, H.S. Kim, and S. Lee: *Mater. Sci. Eng. A*, 2014, vol. 607, pp. 197–205.
28. C. Jeon, C.P. Kim, S.H. Joo, H.S. Kim, and S. Lee: *Acta Mater.*, 2013, vol. 61, pp. 3012–26.
29. W. Chen and B. Song: *Split Hopkinson (Kolsky) Bar*, Springer, Berlin, 2011.
30. J.E. Field, S.M. Walley, W.G. Proud, H.T. Goldrein, and C.R. Siviour: *Int. J. Impact Eng*, 2004, vol. 30, pp. 725–75.
31. J. Harding and L.M. Welsh: *J. Mater. Sci.*, 1983, vol. 18, pp. 1810–26.
32. G.T. Gray, III: *Classic Split-Hopkinson Pressure Bar Testing, ASM Handbook, Mechanical Testing and Evaluation*, ASM International, Materials Park, 2000, pp. 462–76.
33. G.T. Gray, III, and W.R. Blumenthal: Split-Hopkinson Pressure Bar Testing of Soft Materials, ASM Handbook, Mechanical Testing and Evaluation, Materials Park, OH, ASM International, 2000, pp. 488–96.
34. C. Jeon, B.-C. Suh, C. Kim, H. Kim, N. Kim, and S. Lee: *Metall. Mater. Trans. A*, 2015, vol. 46A, pp. 2506–15.
35. Y.-H. Kim, D. Kwon, and S. Lee: *Acta Metall. Mater.*, 1994, vol. 42, pp. 1887–91.
36. M. Kusy, U. Kühn, A. Concustell, A. Gebert, J. Das, J. Eckert, L. Schultz, and M.D. Baro: *Intermetallics*, 2006, vol. 14, pp. 982–86.
37. C. Jeon, D. Ha, C. Kim, and S. Lee: *Metall. Mater. Trans. A*, 2012, vol. 43A, pp. 3663–74.
38. D.Q. Ma, W.T. Jiao, Y.F. Zhang, B.A. Wang, J. Li, X.Y. Zhang, M.Z. Ma, and R.P. Liu: *J. Alloy. Compd.*, 2015, vol. 624, pp. 9–16.
39. R.L. Narayan, P.S. Singh, D.C. Hofmann, N. Hutchinson, K.M. Flores, and U. Ramamurty: *Acta Mater.*, 2012, vol. 60, pp. 5089–5100.
40. R. Ayres and M. Wenner: *Metall. Trans. A*, 1979, vol. 10A, pp. 41–46.